Check for updates

Proceedings of the ASME 2022
International Design Engineering Technical Conferences and
Computers and Information in Engineering Conference
IDETC-CIE2022
August 14-17, 2022, St. Louis, Missouri

DETC2022-91322

Downloaded from http://asmedigitalcollection.asme.org/IDETC-CIE/proceedings-pdf/IDETC-CIE2022/86311/V010T10A013/6944006/v010t10a013-detc2022-91322.pdf by Michigan State University, Wei Che Tai on 05 October 2023

OCEAN WAVE ENERGY CONVERSION OF A SPAR PLATFORM USING A NONLINEAR INERTER PENDULUM VIBRATION ABSORBER

Aakash Gupta, Wei-Che Tai
Department of Mechanical Engineering
Michigan State University
East Lansing, Michigan 48824
e-mail: guptaaa3@msu.edu
e-mail: taiweich@msu.edu

ABSTRACT

A nonlinear inerter pendulum vibration absorber is integrated with an electromagnetic power take-off system (called IPVA-PTO) and is analyzed for its efficacy in ocean wave energy conversion of a spar platform. The IPVA-PTO system shows a nonlinear energy transfer phenomenon between the spar and the IPVA-PTO which can be used to convert the vibration energy of the spar into electricity while reducing the hydrodynamic response of the spar. The hydrodynamic coefficients of the spar are computed using a commercial boundary-element-method (BEM) code. It is shown that the energy transfer is associated with 1:2 internal resonance of the pendulum vibration absorber, which is induced by a period-doubling bifurcation. The period-doubling bifurcation is studied using the harmonic balance method. A modified alternating frequency/time (AFT) approach is developed to compute the Jacobian matrix involving nonlinear inertial effects of the IPVA-PTO system. It is shown that the period-doubling bifurcation leads to 1:2 internal resonance and plays a major role in the energy transfer between the spar and the pendulum. The response amplitude operator (RAO) in heave and the capture width of the IPVA-PTO-integrated spar are compared with its linear counterpart and it is shown that the IPVA-PTO system outperforms the linear energy harvester as the former has a lower RAO and higher capture width.

1 Introduction

Ocean wave energy resources are enormous. It is estimated that the annual average wave power incident on the ocean-facing coastlines of North America is over 400 GW (about 80% electricity consumption for the entire continent [1]). Despite the enormous resources, the cost of using existing wave energy converters (WECs) to generate electricity from ocean waves is higher than solar and wind energy conversion technologies. Costs of installation, mooring/foundation, operation and maintenance account for 40%–50% of wave energy project life costs [2]. A promising way to reduce these costs is to integrate WECs with offshore floating platforms because they can share infrastructure, equipment, mooring and anchoring systems, and survey and monitoring methods [3]. Recently, the oil and gas industry has been investigating the feasibility of converting mature offshore platforms into renewable energy hubs by mounting WECs to the platforms [4]. The WECs can directly supply electricity to the platforms to further lower the cost of wave energy [5].

Offshore floating platforms are worldwide operating in deep water areas for oil and gas production [6] and providing the foundation for floating wind turbines [7]. Specifically, spar platforms establish the buoyancy and stability on a long and slender cylinder that goes deep below the water surface, thereby having good hydrodynamic response/stability and large water depths (600–2500 meters for oil spar platforms in the Gulf of Mexico [8]). On the other hand, heaving WECs convert the relative

Copyright © 2022 by ASME

heave motion between oscillating bodies into electricity and have a high wave energy conversion efficiency when operating at resonance [9]. As the wave energy resources are more abundant in deep water than shallow water, it is reasonable to integrate WECs and spar platforms. Thus far, several researchers have studied the integration of a spar platform and different types of heaving WECs [10–13]. Existing numerical studies [10, 13] suggest that such integration can lead to a 7%–30% capture width ratio (hydrodynamic efficiency) of wave energy production, which is comparable with existing heaving WECs [14]. According to the scaling law in [14], heaving WECs of a larger diameter would have a higher capture width ratio. A typical spar platform in the Gulf of Mexico, e.g., the Horn Mountain, has a diameter of 30 meters (BSEE data [8]). If the spar-WEC integration in [10, 13] were scaled up to this diameter, the peak mean wave power in operational conditions would be 2.4–10 MW (current floating wind turbines have 5–MW wind power).

Although showing promising wave energy conversion, such integration does not assure good hydrodynamic response of the platform. Past studies have shown that the integration with heaving WECs amplifies the platform heave and pitch motion [10–12], and even cause Mathieu instability [15], which would aggravate fatigue of the mooring and riser systems and even lead to failure of the whole system [16, 17]. This deterioration of hydrodynamic response and stability can be explained as follows. Generally speaking, a spar platform has a 20–30 s heave natural period [18, 19] which is far away from typical incident wave periods (5–10 s [20]) to avoid large heave resonant response. On the other hand, traditional heaving WECs operate based on the basic principle of linear resonance, thereby having a natural period in heave close to a typical wave period to generate large heave resonant response and hence high-efficiency wave power production. When a heaving WEC is integrated with a platform, this large heave resonant response can give rise to large platform heave/pitch motions. In other words, wave power production and hydrodynamic response reduction are conflicting objectives in traditional linear WECs.

Recently, Gupta and Tai [21] studied vibration suppression of a nonlinear inerter pendulum vibration absorber (IPVA) which operates based on internal resonance. They found that when the IPVA is incorporated in a structure seeking vibration mitigation, the pendulum can have resonant responses through 1:2 internal resonance while the structure response is suppressed by a saturation-like phenomenon. In this study, the IPVA is integrated with an electromagnetic power take-off (PTO) and applied to an floating spar for wave energy conversion. The PTO-integrated IPVA is referred to as IPVA-PTO hereinafter for brevity.

2 The IPVA-PTO system

Figure 1 shows the IPVA-PTO system mounted between a spar and a fixed frame. The spar (primary structure) is floating in the water, with hydrodynamic stiffness k in the heaving (x) direction. The system consists of a lead screw and nut mounted between a fixed reference and the spar such that the heaving displacement is converted into the angular displacement θ through $x = R\theta$, where $R = L/2\pi$, where L is the screw lead. The carrier is fixed to the screw and has the same angular displacement. The pendulum pivots on a point of the carrier which is located at a distance of R_p from the carrier center. The pendulum length is r and has the angular displacement ϕ with respect to the screw. The planetary gear system is used to combine the pendulum and screw motion into one angular motion $\dot{\theta} - \dot{\phi}$ input to the generator for electricity. A generalized force F_g is the force on the spar, assumed to contain a single harmonic for the current analysis, due to the wave-structure interaction and its derivation is discussed further in Sec. 2.2. The inductance of the generator is neglected because typical wave frequencies are too low for it be significant [22]. This means the electrical power generated by the generator can be written as $\frac{1}{2}c_e\left(\dot{\theta} - \dot{\phi}\right)^2$, where c_e is the electrical damping in the system.

For the purpose of this study, the 1:100 sparD model in [23] is considered. Note that the heaving plate and the mooring lines are ignored and the spar is assumed to have only heaving motion. The mass of the spar M is given as 18.83 kg, the draft d is taken to be 0.96 m and the diameter of the spar $2a$ is 0.16m. The depth of the water is $h = 3$ m and the height of the spar $d + b$ is 1.06 m, which makes the free board $b = 0.1$ m. The wave amplitude is taken to be 6 cm per [23]. The density of water is taken to be $\rho = 1025$ kg/m^3 and acceleration due to gravity $g = 9.81$ m/s^2.

2.1 Equations of motion

We use Lagrange's equations to derive the equations of motion for the IPVA-PTO. The procedure outlined below is similar to the procedure explained in [21]. First, the total kinetic energy of the system is derived as

$$T = T_M + T_c + T_p + T_g \tag{1}$$

where

$$\begin{aligned} T_M &= \frac{1}{2}M\left(R\dot{\theta}\right)^2, \quad T_c = \frac{1}{2}J\dot{\theta}^2, \\ T_p &= \frac{1}{2}J_p\left(\dot{\theta} + \dot{\phi}\right)^2 \\ &\quad + \frac{1}{2}m\left(R_p^2\dot{\theta}^2 + r^2\left(\dot{\theta} + \dot{\phi}\right)^2 + 2R_p r\cos(\phi)\,\dot{\theta}\left(\dot{\theta} + \dot{\phi}\right)\right) \\ T_r &= \frac{1}{2}J_r\left(\dot{\theta} - \dot{\phi}\right)^2 \end{aligned} \tag{2}$$

are the kinetic energy of the spar, carrier, pendulum, and the generator respectively. Here, J is the moment of inertia of the screw

Downloaded from http://asmedigitalcollection.asme.org/IDETC-CIE/proceedings-pdf/IDETC-CIE2022/86311/V010T10A013/6944006/v010t10a013-detc2022-91322.pdf by Michigan State University, Wei Che Tai on 05 October 2023

Copyright © 2022 by ASME

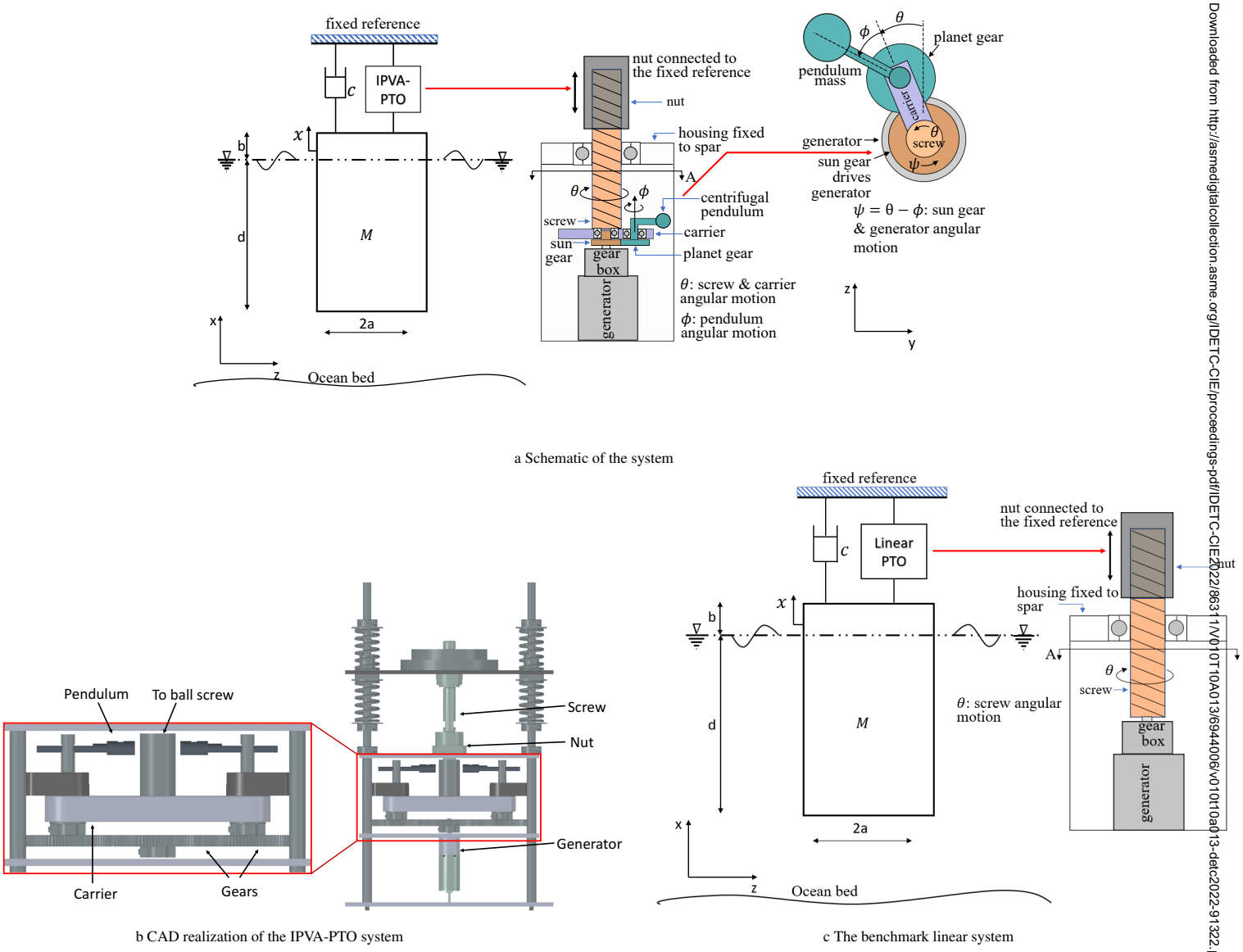

a Schematic of the system

b CAD realization of the IPVA-PTO system

c The benchmark linear system

FIGURE 1: The IPVA-PTO system integrated with a spar: schematic and CAD realization, and the benchmark linear system

and carrier, J_p is the moment of inertia of pendulum with respect to its center of mass, and J_r is the moment of inertia of the rotor of the generator. Furthermore, the potential energy is written as

$$V = \frac{1}{2}kx^2 = \frac{1}{2}kR^2\theta^2. \tag{3}$$

To account for energy loss due to the screw motion, a viscous damping coefficient c is introduced. The virtual work done by the force F_g, the electrical damping torque in the rotor and the viscous damping force can be derived as $F_g\delta x$, $-c_e\left(\dot{\theta}-\dot{\phi}\right)\delta\left(\theta-\phi\right)$ and $-c\dot{x}\delta x$, respectively, where c_e and c are the torsional electrical damping coefficient of the generator [22] and damping coefficient of the viscous damper, respectively. Then the virtual work done by the force F_g, the damping torque (due to c_e and viscous damping c) are derived as

$$\delta W = F_g R\delta\theta - c_e\left(\dot{\theta}-\dot{\phi}\right)\delta\left(\theta-\phi\right) - cR^2\dot{\theta}\delta\theta. \tag{4}$$

The pendulum is assumed to be a point mass; thus, J_p is neglected. Furthermore, the moment of inertia of the screw and

Downloaded from http://asmedigitalcollection.asme.org/IDETC-CIE/proceedings-pdf/IDETC-CIE2022/86311/V010T10A013/6944006/v010t10a013-detc2022-91322.pdf by Michigan State University, Wei Che Tai on 05 October 2023

Copyright © 2022 by ASME

carrier is assumed to be small in comparison with the moment of inertia of other objects in the system; thus, J is neglected. Therefore, the equations of motion of the system obtained using Lagrange's equations are written as

$$\begin{aligned}&\left(MR^2+J_r+mR_p^2+mr^2+2mR_pr\cos\phi\right)\ddot{\theta}\\&+\left(mr^2+mR_pr\cos\phi\right)\ddot{\phi}+cR^2\dot{\theta}+c_e\left(\dot{\theta}-\dot{\phi}\right)\\&+kR^2\theta-2mR_pr\dot{\phi}\dot{\theta}\sin\phi-mR_pr\dot{\phi}^2\sin\phi=F_gR,\\&mr^2\ddot{\phi}+m\left(r^2+R_pr\cos\phi\right)\ddot{\theta}+c_e\left(\dot{\phi}-\dot{\theta}\right)\\&+mR_pr\dot{\theta}^2\sin\phi=0\end{aligned}\tag{5}$$

We rescale the time and convert (5) into a dimensionless form for further analysis using the following parameters,

$$\begin{aligned}&\mu_r=\frac{mR_p^2}{MR^2},\ \omega_0=\sqrt{\frac{k}{M}},\ \omega=\frac{\Omega}{\omega_0},\ \tau=\omega_0t,\ \eta=\frac{r}{R_p},\\&\eta_g=\frac{J_r}{MR^2},\ \xi=\frac{c}{2\omega_0M},\ \xi_e=\frac{c_e}{2\omega_0MR^2},\ f_g=\frac{F_g}{MR\omega_0^2},\\&()'=\frac{d()}{d\tau}.\end{aligned}\tag{6}$$

Let us define $\mathbf{x}=[\theta,\phi]^T$ and $\mathbf{f}_g=[f_g,0]^T$. The dimensionless equations of motion are obtained as

$$\mathbf{M}\mathbf{x}''+\mathbf{C}\mathbf{x}'+\mathbf{K}\mathbf{x}+\mathbf{g}\left(\mathbf{x},\mathbf{x}',\mathbf{x}''\right)=\mathbf{f}_g\tag{7}$$

where

$$\begin{aligned}&\mathbf{M}=\begin{bmatrix}\eta_g+1+\mu_r\left(1+\eta^2\right) & \mu_r\eta^2-\eta_g\\ \mu_r\eta^2-\eta_g & \eta_g+\mu_r\eta^2\end{bmatrix},\\&\mathbf{C}=\begin{bmatrix}2\left(\xi+\xi_e\right) & -2\xi_e\\ -2\xi_e & 2\xi_e\end{bmatrix},\ \mathbf{K}=\begin{bmatrix}1 & 0\\ 0 & 0\end{bmatrix},\\&\mathbf{g}\left(\mathbf{x},\mathbf{x}',\mathbf{x}''\right)=\mu_r\eta\begin{bmatrix}\left(2\theta''+\phi''\right)\cos\phi-\phi'\left(2\theta'+\phi'\right)\sin\phi\\ \theta''\cos\phi+\theta'^2\sin\phi\end{bmatrix}\end{aligned}\tag{8}$$

2.2 Hydrodynamic coefficients

We use the linear wave theory to determine the hydrodynamic coefficients of the spar subject to incident regular waves, which assumes that the fluid is inviscid and irrotational. Based on the theory, the hydrodynamic force on the spar consists of three components: Froude-Krylov force, diffraction force, and radiation force. The first two correspond to the incident wave field without and with the spar, respectively, and the last one is due to the oscillation of the spar.

The Froude-Krylov and diffraction force together give rise to the excitation force while the radiation force gives rise to the added mass and radiation damping [20, 24], which can be represented by the well-known Cummins' equation [25]:

$$F_g=-A_\infty\ddot{x}-\int_{\sigma=0}^{\infty}k_R\left(\sigma\right)\dot{x}\left(t-\sigma\right)d\sigma+\gamma F_e(t)\tag{9}$$

where γ is the wave amplitude, F_e is the excitation force per wave amplitude, and the radiation impulse response kernel, $k_R\left(\sigma\right)$, and the radiation infinite-frequency added mas, A_∞, are related to the radiation frequency-dependent damping and added mass $B_R\left(\Omega\right)$ and $A_R\left(\Omega\right)$, through Ogilvie's relations [26]

$$\begin{aligned}B_R\left(\Omega\right)&=\int_{\sigma=0}^{\infty}k_R\left(\sigma\right)\cos\left(\Omega\sigma\right)d\sigma\\A_R\left(\Omega\right)&=A_\infty-\frac{1}{\Omega}\int_{\sigma=0}^{\infty}k_R\left(\sigma\right)\sin\left(\Omega\sigma\right)d\sigma\end{aligned}\tag{10}$$

and

$$A_\infty=\lim_{\Omega\to\infty}A_R\left(\Omega\right)\tag{11}$$

After substituting (10) and (11) into (7) and using (6), the equation of motion now becomes

$$\begin{aligned}&\left(\mathbf{M}+\mathbf{A}_\infty\right)\mathbf{x}''+\mathbf{C}\mathbf{x}'+\int_{s=0}^{\infty}\mathbf{K}_R\left(s\right)\mathbf{x}'\left(\tau-s\right)ds+\mathbf{K}\mathbf{x}\\&+\mathbf{g}\left(\mathbf{x},\mathbf{x}',\mathbf{x}''\right)=\mathbf{f}\end{aligned}\tag{12}$$

In (12),

$$\mathbf{A}_\infty=\begin{bmatrix}\frac{A_\infty}{M} & 0\\ 0 & 0\end{bmatrix},\ \mathbf{K}_R\left(s\right)=\begin{bmatrix}\kappa_R\left(s\right) & 0\\ 0 & 0\end{bmatrix},\ \mathbf{f}=\begin{Bmatrix}f_e\left(\tau\right)\\ 0\end{Bmatrix}\tag{13}$$

where $s=\omega_0\sigma$ is the normalized time, $\kappa_R\left(s\right)=k_R\left(s/\omega_0\right)/\left(M\omega_0^2\right)$ is the normalized radiation impulse response kernel, and $f_e=\gamma F_e/\left(MR\omega_0^2\right)$ is the dimensionless excitation force.

2.3 Determination of hydrodynamic coefficients

The hydrodynamic coefficients, Froude-Krylov and diffraction force are determined using Ansys AQWA. A convergence test is conducted to match the published results in [27]. A particular case with $a=0.2$ m, $h=1$ m, and $d=0.25$ m is chosen. Fig. 2 shows the comparison between the added mass and radiation damping between Ansys and the published results. Note that

Downloaded from http://asmedigitalcollection.asme.org/IDETC-CIE/proceedings-pdf/IDETC-CIE2022/86311/V010T10A013/6944006/v010t10a013-detc2022-91322.pdf by Michigan State University, Wei Che Tai on 05 October 2023

Copyright © 2022 by ASME

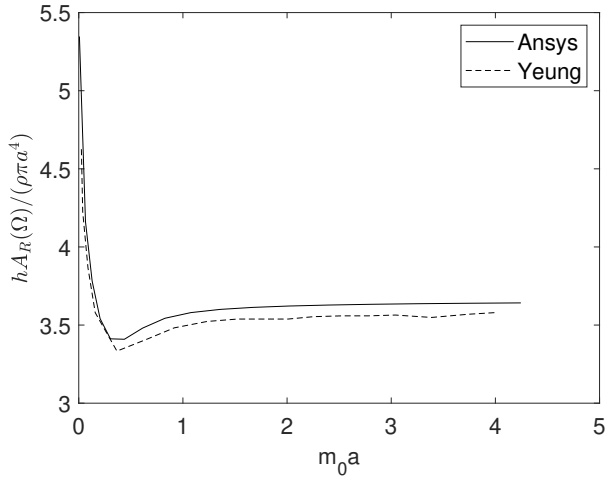

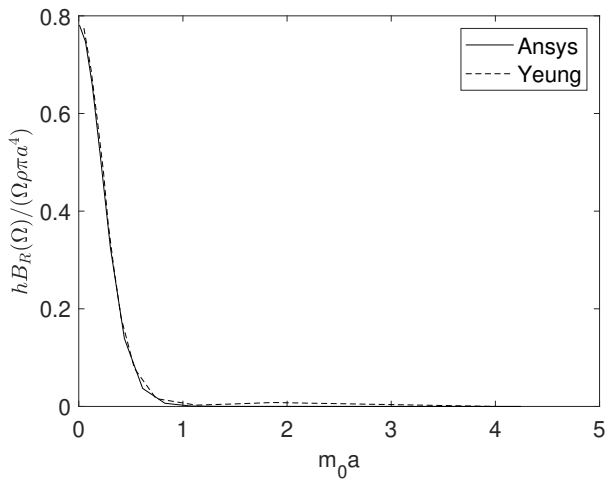

b Radiation damping comparison

FIGURE 2: Comparison of added mass and radiation damping between Yeung et al. [27] and Ansys simulation for $a = 0.2$m, $h = 1$m, $d = 0.25$m

m_0 is the solution to the equation

$$m_0 \tanh(m_0) = \frac{\Omega^2 h}{g} \tag{14}$$

From Fig. 2a and Fig. 2b, it can be observed that the Ansys solutions and the published results are in close agreement with each other. After verifying the Ansys model, we adopt the same setting to simulate the sparD system with the parameters provided in Sec. 2. Fig. 3 shows the mesh of the system used for analysis and Fig. 4 shows the added mass, radiation damping, and excitation force obtained using Ansys for sparD.

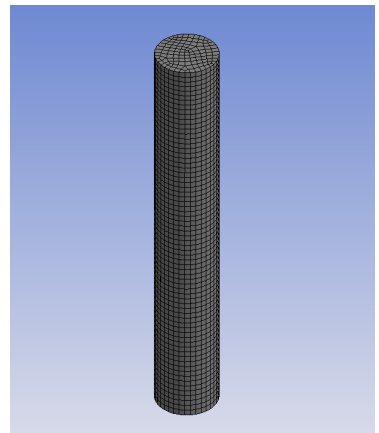

FIGURE 3: Ansys AQWA model for calculation of hydrodynamic coefficients

3 Internal resonance and bifurcation boundaries

Internal resonance has been shown to be essential for nonlinear vibration absorbers to absorb vibration energy of a primary structure they are attached to [21, 28–30]. To investigate internal resonance of the IPVA-PTO system, we will first determine the conditions required to have internal resonance using the harmonic balance method in conjunction with the modified alternating frequency/time approach discussed in Section 3.2. The convolution terms are handled separately as discussed in Section 3.3. Specifically, 1:2 internal resonance will be the focus in the analysis as it has been shown to achieve energy absorption from an oscillating structure seeking vibration mitigation in the authors' past study [21]. In this study, we use the harmonic balance method to investigate internal resonance.

3.1 Harmonic balance analysis

In a fashion similar to [21], we assume the periodic solutions of the system take the form

$$\theta_p(\tau) = \Theta_0 + \sum_{p=1}^{P}\left[\Theta_p^c \cos\left(\frac{p\omega\tau}{\nu}\right) + \Theta_p^s \sin\left(\frac{p\omega\tau}{\nu}\right)\right],$$
$$\phi_p(\tau) = \Phi_0 + \sum_{p=1}^{P}\left[\Phi_p^c \cos\left(\frac{p\omega\tau}{\nu}\right) + \Phi_p^s \sin\left(\frac{p\omega\tau}{\nu}\right)\right] \tag{15}$$

where Θ_p, Φ_p, Θ_0 and Φ_0 are unknown Fourier coefficients to be determined. As has been reported previously [21], Φ_0 is included to consider asymmetric pendulum oscillations [31], whereas Θ_0 is introduced to expedite the derivation. It is found that $\Theta_0 = 0$ as the spar oscillates symmetrically with respect to the free surface. On the other hand, a nonzero Φ_0 is necessary for 1:2 internal resonance [21]. Next, we substitute (15) into (12) to obtain the

Downloaded from http://asmedigitalcollection.asme.org/IDETC-CIE/proceedings-pdf/IDETC-CIE2022/86311/V010T10A013/6944006/v010t10a013-detc2022-91322.pdf by Michigan State University, Wei Che Tai on 05 October 2023

Copyright © 2022 by ASME

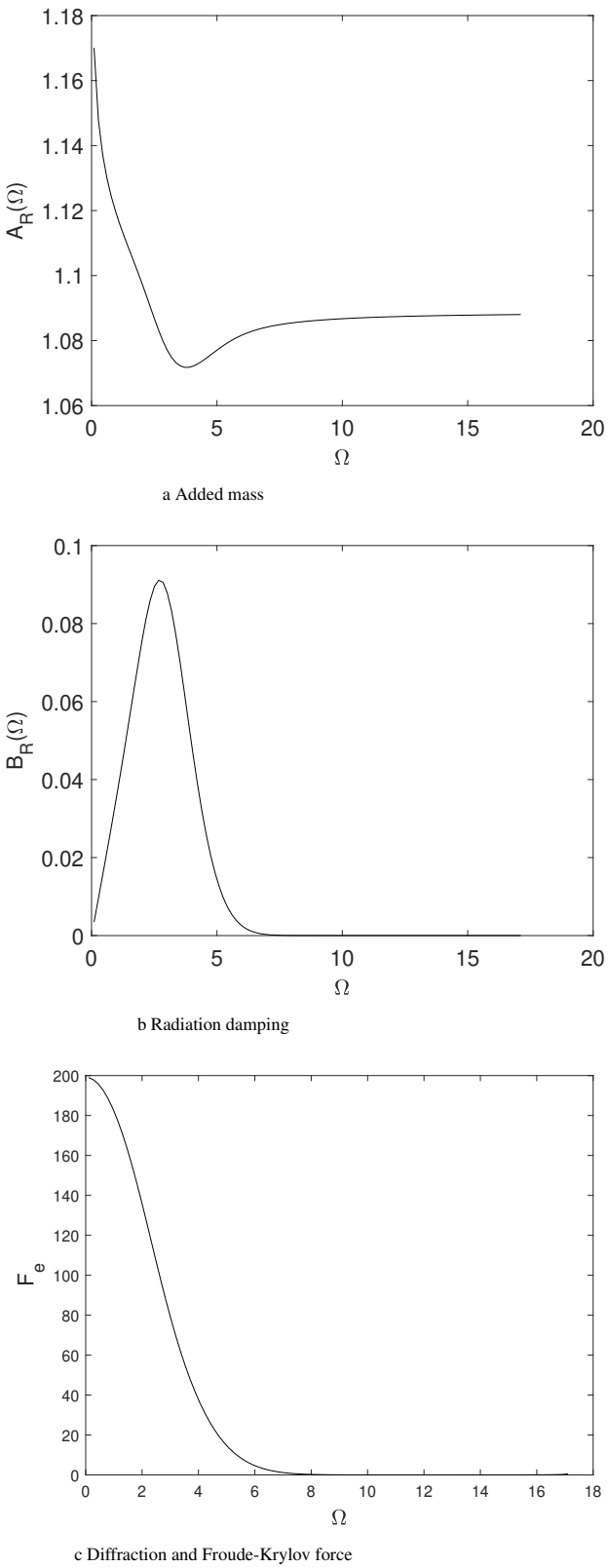

FIGURE 4: Added mass, radiation damping and diffraction and Froude-Krylov force for sparD

residue term

$$\mathbf{R}(\tau) = \mathbf{M}\mathbf{x}_p'' + \mathbf{C}\mathbf{x}_p' + \int_{s=0}^{\infty} \mathbf{K}_R(s)\,\mathbf{x}'(\tau - s)\,ds + \mathbf{K}\mathbf{x}_p - \mathbf{g}\left(\mathbf{x}_p, \mathbf{x}_p', \mathbf{x}_p''\right) - \mathbf{f}. \tag{16}$$

where $\mathbf{x}_p = [\theta_p, \phi_p]^T$ is the assumed solution vector. Using Galerkin's projection on the orthogonal trigonometric basis, we can obtain

$$\begin{aligned} h_0(\mathbf{X}) &= \int_0^{\frac{2\pi\nu}{\omega}} \mathbf{R}(\tau)d\tau = 0, \\ h_p^s(\mathbf{X}) &= \int_0^{\frac{2\pi\nu}{\omega}} \mathbf{R}(\tau)\sin\left(\frac{p\omega\tau}{\nu}\right)d\tau = 0, \\ h_p^c(\mathbf{X}) &= \int_0^{\frac{2\pi\nu}{\omega}} \mathbf{R}(\tau)\cos\left(\frac{p\omega\tau}{\nu}\right)d\tau = 0 \end{aligned} \tag{17}$$

where $\mathbf{X} = [\mathbf{X}_0,\ \mathbf{X}_1^c,\ \mathbf{X}_1^s, \ldots, \mathbf{X}_p^c,\ \mathbf{X}_p^s]^T$, where $\mathbf{X}_0 = [\Theta_0, \Phi_0]$, $\mathbf{X}_1^c = [\Theta_1^c, \Phi_1^c]$, $\mathbf{X}_1^s = [\Theta_1^s, \Phi_1^s]$, and so on. Eqn. (17) is a set of nonlinear algebraic equations and can be solved by iterative methods like the Newton-Raphson scheme. However, since the term $\mathbf{g}\left(\mathbf{x}_p, \mathbf{x}_p', \mathbf{x}_p''\right)$ will result in composite trigonometric terms such as $\cos\left(\Phi_p^s \sin\left(p\omega\tau/\nu\right)\right)$, one needs to use special expansions (example, using Bessel functions) to extract the Fourier coefficients of $\mathbf{g}$ (denoted by $\mathbf{G}$). Moreover, for stability analysis, one would require to compute the Jacobian matrix $\frac{\partial \mathbf{G}}{\partial \mathbf{X}}$, which is computationally expensive in the frequency domain. To that end, we use a modification of the alternating frequency/time domain (AFT) method [32–34] to compute the value of $\mathbf{G}$ and $\frac{\partial \mathbf{G}}{\partial \mathbf{X}}$. Furthermore, to apply the harmonic balance method, we would require to obtain the Fourier coefficients of the convolution term. This calculation is explained in Section 3.3.

3.2 Modified alternating frequency/time approach

We follow the AFT algorithm as implemented in [34] with a slight modification which takes care of nonlinear inertia. Let us define $\bar{\omega} = \frac{\omega}{\nu}$ and expand the nonlinear function by Fourier series such that

$$\mathbf{g}\left(\mathbf{x}_p, \mathbf{x}_p', \mathbf{x}_p''\right) = \mathbf{G}_0 + \sum_{p=1}^{P} \left(\mathbf{G}_p^c \cos\left(p\bar{\omega}\tau\right) + \mathbf{G}_p^s \sin\left(p\bar{\omega}\tau\right)\right)$$

which can be rewritten as

$$\mathbf{g}\left(\mathbf{x}_p, \mathbf{x}_p', \mathbf{x}_p''\right) = \left(\mathbf{T}\left(\bar{\omega}\tau\right) \otimes I_n\right)\mathbf{G}$$

Downloaded from http://asmedigitalcollection.asme.org/IDETC-CIE/proceedings-pdf/IDETC-CIE2022/86311/V010T10A013/6944006/v010t10a013-detc2022-91322.pdf by Michigan State University, Wei Che Tai on 05 October 2023

Copyright © 2022 by ASME

where

$$\mathbf{T}(\bar{\omega}\tau) = [1\ \cos(\bar{\omega}\tau)\ \sin(\bar{\omega}\tau) \ldots \cos(P\bar{\omega}\tau)\ \sin(P\bar{\omega}\tau)]$$
$$\mathbf{G} = [\mathbf{G}_0^T,\ (\mathbf{G}_1^c)^T,\ (\mathbf{G}_1^s)^T, \ldots, (\mathbf{G}_P^c)^T,\ (\mathbf{G}_P^s)^T]^T \tag{18}$$

where $\otimes$ is the Kronecker tensor product and I_n is the $n \times n$ identity matrix. Similarly,

$$\mathbf{x} = (\mathbf{T}(\bar{\omega}\tau) \otimes I_n)\mathbf{X}$$

where $\mathbf{X}$ is the vector consisting of all retaining Fourier coefficients; see (17).

The AFT method finds the time domain value of the nonlinear function and transforms it back to the frequency domain, i.e.

$$\mathbf{X} \xrightarrow{DFT^{-1}} \mathbf{x}_p(t),\ \mathbf{x}_p(t)',\ \mathbf{x}_p(t)'' \longrightarrow \mathbf{g}\left(\mathbf{x}_p, \mathbf{x}_p', \mathbf{x}_p''\right) \xrightarrow{DFT} \mathbf{G}(\mathbf{X}) \tag{19}$$

where DFT represents the discrete Fourier transform. Taking N uniformly separated time points, $t_i = \frac{2\pi i}{\omega N}$, and defining the vectors

$$\bar{\mathbf{x}} = \left[\mathbf{x}_p^T(t_1), \mathbf{x}_p^T(t_2) \ldots, \mathbf{x}_p^T(t_N)\right]^T \tag{20}$$
$$\bar{\mathbf{g}} = \left[\mathbf{g}^T(t_1), \mathbf{g}^T(t_2) \ldots, \mathbf{g}^T(t_N)\right]^T. \tag{21}$$

and

$$\mathbf{U} = \begin{bmatrix} 1 & \cos\left(\frac{2\pi}{N}\right) & \sin\left(\frac{2\pi}{N}\right) & \ldots & \cos\left(\frac{2\pi P}{N}\right) & \sin\left(\frac{2\pi P}{N}\right) \\ \vdots & \vdots & \vdots & & & \\ 1 & \cos\left(\frac{2\pi N}{N}\right) & \sin\left(\frac{2\pi N}{N}\right) & \ldots & \cos\left(\frac{2\pi PN}{N}\right) & \sin\left(\frac{2\pi PN}{N}\right) \end{bmatrix},$$

the Fourier coefficients can be computed using

$$\mathbf{G} = \left(\mathbf{U}^{-1} \otimes \mathbf{I}_n\right)\bar{\mathbf{g}} \tag{22}$$
$$\mathbf{X} = \left(\mathbf{U}^{-1} \otimes \mathbf{I}_n\right)\bar{\mathbf{x}} \tag{23}$$

where

$$\mathbf{U}^{-1} = 1/N \begin{bmatrix} 1 & \ldots & 1 \\ 2\cos(\frac{2\pi}{N}) & \ldots & 2\cos(\frac{2\pi N}{N}) \\ 2\sin(\frac{2\pi}{N}) & \ldots & 2\sin(\frac{2\pi N}{N}) \\ \vdots & \vdots & \vdots \\ 2\cos(\frac{2\pi P}{N}) & \ldots & 2\cos(\frac{2P\pi N}{N}) \\ 2\sin(\frac{2\pi P}{N}) & \ldots & 2\sin(\frac{2P\pi N}{N}) \end{bmatrix} \tag{24}$$

is the Moore-Penrose pseudo-inverse of $\mathbf{U}$. Also,

$$\bar{\mathbf{x}}' = \omega\left(\mathbf{U}\nabla \otimes \mathbf{I}_n\right)X, \tag{25}$$
$$\bar{\mathbf{x}}'' = \omega^2\left(\mathbf{U}\nabla^2 \otimes \mathbf{I}_n\right)X, \tag{26}$$

where

$$\nabla = \begin{bmatrix} \mathbf{0} & & & & \\ & \ddots & & & \\ & & \nabla_i & & \\ & & & \ddots & \\ & & & & \nabla_P \end{bmatrix}, \quad \nabla_i = \begin{bmatrix} 0 & i \\ -i & 0 \end{bmatrix}. \tag{27}$$

Thus, the Jacobian matrix of $\mathbf{G}$ can be obtained through

$$\begin{aligned} &\frac{\partial \mathbf{G}}{\partial X} \\ &= \left(\mathbf{U}^{-1} \otimes \mathbf{I}_n\right)\frac{\partial \bar{\mathbf{g}}}{\partial \bar{\mathbf{x}}}\left(\mathbf{U} \otimes \mathbf{I}_n\right) + \left(\mathbf{U}^{-1} \otimes \mathbf{I}_n\right)\frac{\partial \bar{\mathbf{g}}}{\partial \bar{\mathbf{x}}'}\omega\left[(\mathbf{U}\nabla) \otimes \mathbf{I}_n\right] \\ &+ \left(\mathbf{U}^{-1} \otimes \mathbf{I}_n\right)\frac{\partial \bar{\mathbf{g}}}{\partial \bar{\mathbf{x}}''}\omega^2\left[\left(\mathbf{U}\nabla^2\right) \otimes \mathbf{I}_n\right], \end{aligned}$$

where

$$\frac{\partial \bar{\mathbf{g}}}{\partial \mathbf{r}} = \begin{bmatrix} \left.\frac{\partial \bar{\mathbf{g}}}{\partial \mathbf{r}}\right|_{t=t_1} & & \\ & \ddots & \\ & & \left.\frac{\partial \bar{\mathbf{g}}}{\partial \mathbf{r}}\right|_{t=t_N} \end{bmatrix} \tag{28}$$

are the Jacobian of the nonlinear function $\mathbf{g}$ in the time domain and $\mathbf{r}$ can be $\bar{\mathbf{x}}$, $\bar{\mathbf{x}}'$ and $\bar{\mathbf{x}}''$.

3.3 Fourier coefficients of the convolution term

We use the method described in [24] to obtain the Fourier coefficients of the convolution term. After substituting (15) into the convolution term, one arrives at

$$\begin{aligned} I = \int_0^\infty \kappa_R(s) \sum_{p=1}^{P} p\bar{\omega}[&-\Theta_p^c \sin(p\bar{\omega}(\tau - s)) \\ &+ \Theta_p^s \cos(p\bar{\omega}(\tau - s))]ds \end{aligned} \tag{29}$$

where $I = \int_0^\infty \kappa_R(s)\,\theta_p'(\tau - s)\,ds$. Expanding the trigonometric functions and using (10) lead to

$$\begin{aligned} I = &\sum_{p=1}^{P} \bar{\omega}_p\left[-\Theta_c 2\xi_B^{(p)}(\omega_0\bar{\omega}_p) + \Theta_s\bar{\omega}_p\mu_A^{(p)}(\omega_0\bar{\omega}_p)\right]\sin(\bar{\omega}_p\tau) \\ &+ \bar{\omega}_p\left[\Theta_c\bar{\omega}_p\mu_A^{(p)}(\omega_0\bar{\omega}_p) + \Theta_s 2\xi_B^{(p)}(\omega_0\bar{\omega}_p)\right]\cos(\bar{\omega}_p\tau) \end{aligned} \tag{30}$$

Copyright © 2022 by ASME

Downloaded from http://asmedigitalcollection.asme.org/IDETC-CIE/proceedings-pdf/IDETC-CIE2022/86311/V010T10A013/6944006/v010t10a013-detc2022-91322.pdf by Michigan State University, Wei Che Tai on 05 October 2023

where

$$\bar{\omega}_p = p\bar{\omega},\ \ \mu_A^{(p)}(\bar{\omega}_p) = \frac{A_\infty - A_R(\omega_0\bar{\omega}_p)}{M},$$
$$2\xi_B^{(p)}(\bar{\omega}_p) = \frac{B_R(\omega_0\bar{\omega}_p)}{M\omega_0}. \tag{31}$$

Substituting (30) into (17) leads to the Fourier coefficients of the convolution term.

3.4 Stability of the periodic solutions

When the nonlinearity in the system is weak, the periodic solutions (15) are dominated by the primary harmonics. Therefore, $\nu = 1$, $p = 1$ are chosen in this study. We determine the stability of the periodic solutions by introducing small perturbations in (15) as follows:

$$\theta(\tau) = \theta_p(\tau) + \delta_\theta(\tau) \text{ and } \phi(\tau) = \phi_p(\tau) + \delta_\phi(\tau) \tag{32}$$

where $|\delta_\theta(\tau)| << 1$ and $|\delta_\phi(\tau)| << 1$. Let us define $\delta = \left[\delta_\theta, \delta_\phi\right]^T$. Substitution of (32) into (12) and linearization with respect to $\theta_p(\tau)$ and $\phi_p(\tau)$ yield

$$\left(\mathbf{M} + \mathbf{A}_\infty + \frac{\partial \mathbf{g}}{\partial \mathbf{x}''}\right)\delta'' + \left(\mathbf{C} + \frac{\partial \mathbf{g}}{\partial \mathbf{x}'}\right)\delta'$$
$$+ \int_{\tau=0}^{\infty} \mathbf{K}_R(s)\,\delta'(\tau - s)\,ds + \left(\mathbf{K} + \frac{\partial \mathbf{g}}{\partial \mathbf{x}}\right)\delta = \mathbf{0} \tag{33}$$

where the Jacobian matrices $\partial\mathbf{g}/\partial\mathbf{x}''$, $\partial\mathbf{g}/\partial\mathbf{x}'$, and $\partial\mathbf{g}/\partial\mathbf{x}$ are evaluated at $\mathbf{x} = \mathbf{x}_p$, $\mathbf{x}' = \mathbf{x}'_p$, and $\mathbf{x}'' = \mathbf{x}''_p$ using the AFT method described in Section 3.2. Eqn. (33) is a set of linear ordinary differential equations of periodic coefficients. One can use Floquet theory to determine the stability. To this end, (33) is transformed into the state-space form and numerically integrated over one period T to obtain the fundamental matrix. It is, however, difficult to numerically integrate the convolution term. To overcome this difficulty, we use the method illustrated in [35] to obtain a state-space representation that governing the dynamics of the convolution term, which is briefly explained as follows.

Denote by $y(\tau)$ the convolution term in (33), i.e.

$$y(\tau) = \int_0^\infty \kappa_R(s)\,\delta'_\theta(\tau - s)\,ds = \int_{-\infty}^{t} \kappa_R(\tau - s)\,\delta'_\theta(s)\,ds$$

which, after Laplace transform, gives,

$$\tilde{y}(\tilde{s}) = \tilde{H}(\tilde{s})\,\tilde{\delta}'_\theta(\tilde{s})$$

where $\tilde{y}$ and $\tilde{\delta}'$ are the Laplace transform of $y(\tau)$ and $\delta'(\tau)$ respectively, and $\tilde{H}(\tilde{s}) = \int_0^\infty \kappa_R(\tau)\,e^{\tilde{s}\tau}d\tau$. Using this transfer function, we find a state-space realization of order n with state variable $\delta_\theta(\tau)$ and matrices $\mathbf{A} \in \mathbb{R}^{n\times n}$, $\mathbf{B} \in \mathbb{R}^{n\times 1}$, $\mathbf{C} \in \mathbb{R}^{1\times n}$ and $D \in \mathbb{R}$, such that

$$\mathbf{w}'(\tau) = \mathbf{A}\mathbf{w}(\tau) + \mathbf{B}\delta'_\theta(\tau)$$
$$y(\tau) = \mathbf{C}\mathbf{w}(\tau) + D\delta'_\theta(\tau) \tag{34}$$

The state space conversion mentioned above can be achieved using **imp2ss** function in Matlab. To use **imp2ss**, $\kappa_R(\tau)$ can be calculated using (10). We can further reduce the above state space model using **balmr** function in Matlab. After getting a reduced state space model for the convolution integral, the convolution term can be characterized by the state space model (34). As stated previously, when the nonlinearity is weak, the solutions are dominated by the primary harmonics. Therefore, we determine the stability of the primary harmonics. Specifically, we will determine when the primary harmonics undergo period-doubling bifurcation. When this occurs, the system will have 1:2 internal resonance [21, 28–30].

3.5 Periodic doubling bifurcation

We use the bifurcation tracking algorithm developed in [21] to obtain the bifurcation boundary for period-doubling bifurcation in the $f_e - \omega$ plane. The bifurcation boundary for a set of parameters is shown in Fig. 5. When this bifurcation occurs, the pendulum oscillations will have harmonics of $\omega/2$, i.e. 1:2 internal resonance. It is worth noting that autoparametric vibration absorbers also use 1:2 internal resonance to achieve vibration energy absorption [28–30].

4 Numerical demonstration

We now perform direction numerical simulation on the system (using Matlab's ODE45) to verify the bifurcation boundary obtained in Section 3.5. We solve (12) at three points marked in Fig. 5 ($\times$1, $\times$2 and $\times$3). To solve the system numerically, we obtain the state space representation of the convolution term in (12) in a way similar to one described in Section 3.4, and thus giving

$$\tilde{\mathbf{w}}'(\tau) = \tilde{\mathbf{A}}\tilde{\mathbf{w}}(\tau) + \tilde{\mathbf{B}}\theta'(\tau)$$
$$z(\tau) = \tilde{\mathbf{C}}\tilde{\mathbf{w}}'(\tau) + \tilde{D}\theta'(\tau) \tag{35}$$

where $z(\tau) \approx \int_0^\infty \kappa_R(s)\theta'(\tau - s)\,ds$.

As can be observed from Fig. 6a, Fig. 6b, Fig. 7a, Fig. 7b, Fig. 8a, and Fig. 8b, points $\times$1 and $\times$2 lead to periodic solutions whereas point $\times$3 leads to non-periodic solutions. This can be

Downloaded from http://asmedigitalcollection.asme.org/IDETC-CIE/proceedings-pdf/IDETC-CIE2022/86311/V010T10A013/6944006/v010t10a013-detc2022-91322.pdf by Michigan State University, Wei Che Tai on 05 October 2023

Copyright © 2022 by ASME

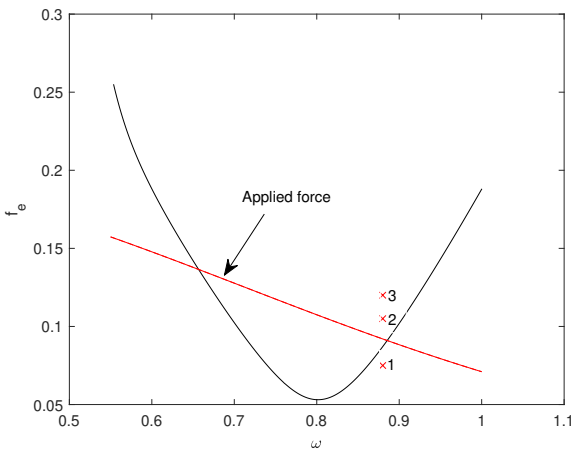

FIGURE 5: Parametric instability boundary for $\eta = 0.4$, $\mu_r = 0.4$, $\eta_g = 0.03$, $\xi = 0.05$, $\xi_p = 0.01$

validated with the fast Fourier transform (FFT) of the solutions at these three points, which is shown in Fig. 6c, Fig. 7c and Fig. 8c, respectively. Note that the frequencies $\hat{\omega}$ of the FFT are normalized with respect to the excitation frequency. Thus, primary harmonics correspond to components at $\hat{\omega} = 1$, harmonics of half excitation frequency correspond to components at $\hat{\omega} = 0.5$, and so on.

In Fig. 5, it can be seen that the point $\times 1$ is below the bifurcation boundary. We expect the solutions to be periodic and dominated by the primary harmonic, which is verified by Fig. 6. Now, as we increase the value of f_e to reach point $\times 2$, a period doubling bifurcation occurs and we expect harmonics of frequency $\omega/2$. This claim is readily verified from Fig. 7, where subharmonics of half excitation frequency indeed exist. As such, it is found that the pendulum has 1:2 internal resonance at point $\times 2$. Finally, the parameters at $\times 3$ lead to strong non-periodic solutions composed of both oscillation and intermittent rotations of the pendulum, as shown in Fig. 8a. This is similar to the non-periodic solutions observed in autoparametric resonance vibration absorbers [30].

5 Discussion

In this study, we investigate how 1:2 internal resonance of the IPVA-PTO can be exploited for wave energy conversion. To show the efficacy of the system, we compare it with a linear wave energy converter. The linear system is characterized by a linear wave energy converter that is obtained by removing the pendulum from the IPVA, as shown in Fig. 1c. We tune the linear inerter to the same natural frequency as the IPVA for a more fairer comparison. This is achieved by increasing the inertance of the generator. Considering the other physical parameters same as the IPVA-PTO, the equation of motion of the linear system will be

$$M_l\theta'' + C_l\theta' + \int_{\tau=0}^{\infty} \kappa_R(s)\,\theta'(\tau - s)\,ds + K_l\theta = f_e \tag{36}$$

where

$$M_l = 1 + \eta_g + \mu_{A\infty} + \mathscr{M},\ \mu_{A\infty} = \frac{A_\infty}{M},\ C_l = 2(\xi + \xi_e),\quad K_l = 1. \tag{37}$$

and $\mathscr{M}$ is the additional inertia used for resonant frequency matching. We solve this system with the method described in Section 3.4 and compare it with the IPVA-PTO system. Note that the excitation force is also frequency dependent. For the current study, we fix the value of R to 28 cm. Fig. 5 shows the force as a variation of normalized angular frequency of the system. When the excitation force magnitude is above the bifurcation boundary, we expect that the vibration energy of the spar transfers to the IPVA. To see that, we compare the response amplitude operator (RAO) in heave and the normalized power of the IPVA-PTO and the linear system. The RAO is defined as

$$RAO = \frac{R\theta}{\gamma}, \tag{38}$$

and the capture width is defined as

$$P = P_{IPVA-PTO}/P_{linear} \tag{39}$$

which is the ratio of the power that the IPVA-PTO converts over the power that the linear benchmark converts. The instantaneous converted wave power for the IPVA and linear system are prospectively written as

$$P_{IPVA-PTO} = c_e(\dot{\theta} - \dot{\phi})^2 \qquad P_{linear} = c_e(\dot{\theta})^2 \tag{40}$$

In this work, the root-mean-square (rms) of the converted power for 600 wave periods is computed for both the linear and nonlinear system. As can be seen from flattening of the oscillations in Fig. 9a (saturation like phenomenon as previously reported in [21]) of the spar and the increase in the capture width within the same frequency range in Fig. 9b, there is an energy transfer from the spar to the pendulum. Note that the capture width is normalized by the maximum of the linear system such for an easy reference. Furthermore, it can be clearly observed from

Downloaded from http://asmedigitalcollection.asme.org/IDETC-CIE/proceedings-pdf/IDETC-CIE2022/86311/V010T10A013/6944006/v010t10a013-detc2022-91322.pdf by Michigan State University, Wei Che Tai on 05 October 2023

Copyright © 2022 by ASME

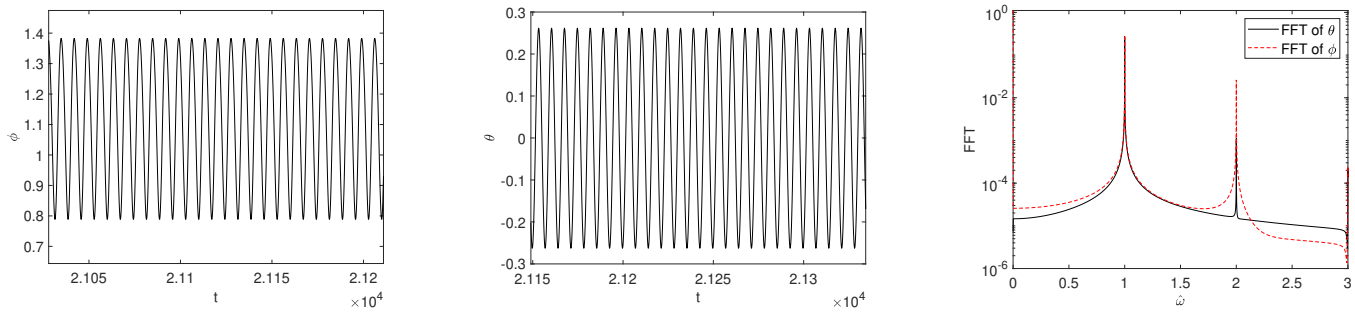

a Time series of ϕ at point 1 b Time series of θ at point 1 c FFT at point 1

FIGURE 6: FFT and time series of periodic solutions at point 1 in Fig. 5

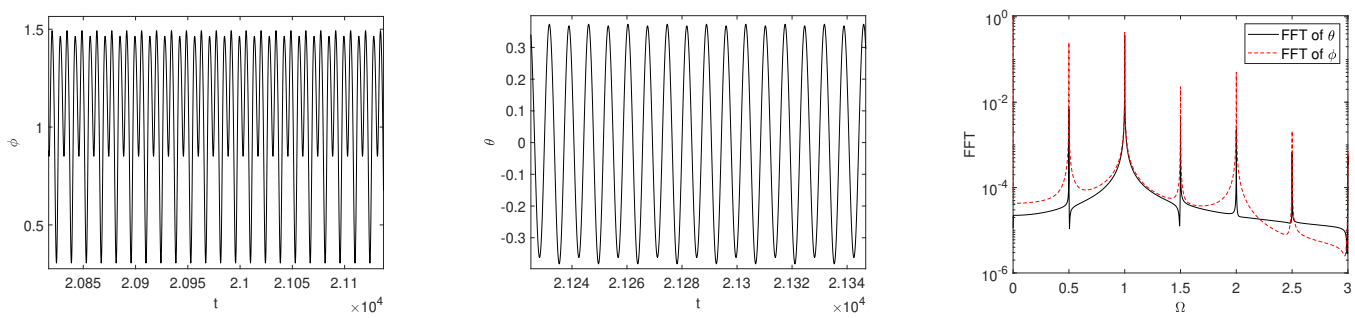

a Time series of ϕ at point 2 b Time series of θ at point 2 c FFT at point 2

FIGURE 7: FFT and time series of periodic solutions at point 2 in Fig. 5

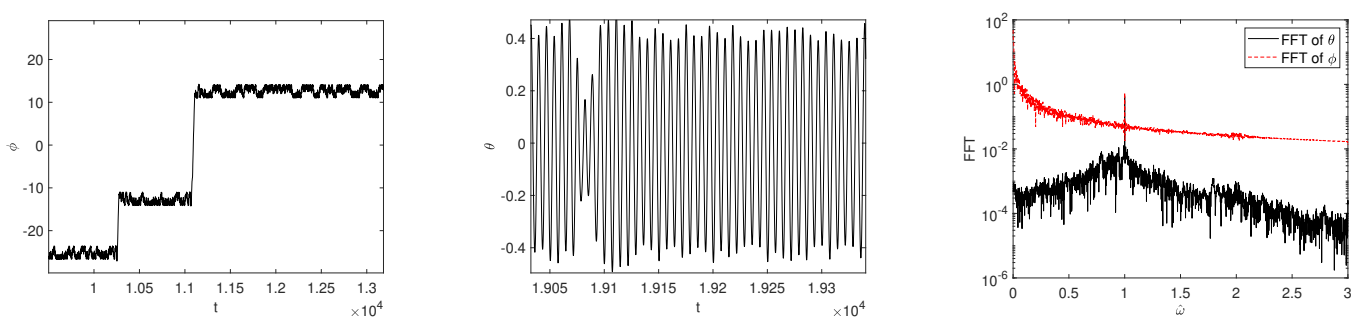

a Time series of ϕ at point 3 b Time series of θ at point 3 c FFT at point 3

FIGURE 8: FFT and time series of periodic solutions at point 3 in Fig. 5

Fig. 9b that the IPVA-PTO system significantly outperforms the linear system. Note that in Fig. 9a, approximately between $\Omega \in [2.3, 2.8]$, there is a presence of chaotic-like motions. The figures represent one such instance of the initial conditions.

6 Conclusion

This study analyzes the modification of the IPVA system [21] with an added generator (referred as IPVA-PTO) for wave energy conversion. The IPVA-PTO is integrated with a spar and the dynamics of the system is analyzed. It is observed that a nonlinear energy transfer phenomenon similar to that observed in [21] exists in the IPVA-PTO system too. It is also shown that because of this energy transfer phenomenon, the IPVA-PTO system is shown to outperform its linear counterpart in terms of the wave capture width.

Note that this is a pilot study where only a spar and a fixed reference is considered. Future work will incorporate the integra-

Downloaded from http://asmedigitalcollection.asme.org/IDETC-CIE/proceedings-pdf/IDETC-CIE2022/86311/V010T10A013/6944006/v010t10a013-detc2022-91322.pdf by Michigan State University, Wei Che Tai on 05 October 2023

Copyright © 2022 by ASME

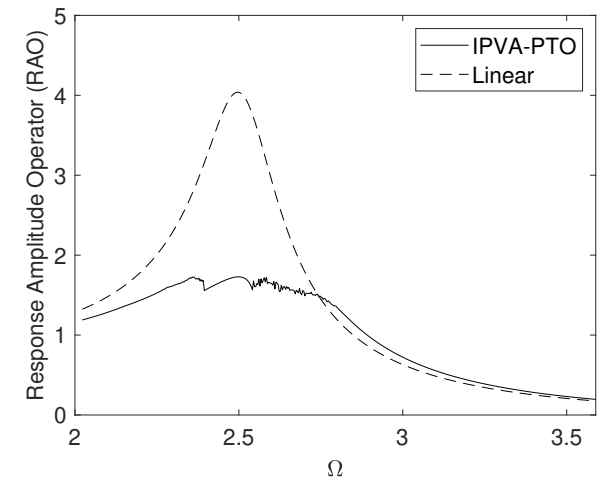

a Comparison of primary oscillation

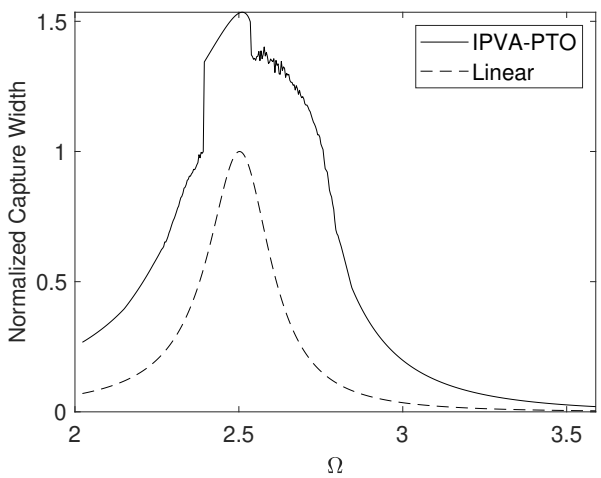

b Normalized capture width of the IPVA-PTO system and the linear system with respect to different angular frequencies

FIGURE 9: Comparison of RAO and capture width between the IPVA-PTO and linear system

tion of spar with a floater integrated with the IPVA-PTO system. There will more rigorous study on chaotic-like motions of Fig. 9a and Fig. 9b.

REFERENCES

[1] Gunn, K., and Stock-Williams, C., 2012. "Quantifying the global wave power resource". *Renewable Energy,* **44**, pp. 296–304.

[2] Bedard, R., Hagerman, G., Previsic, M., Siddiqui, O., Thresher, R., and Ram, B., 2005. "Final summary report, project definition study, offshore wave power feasibility demonstration project". *Electric Power Research Institute Inc*.

[3] Nguyen, H., Wang, C., Tay, Z., and Luong, V., 2020. "Wave energy converter and large floating platform integration: A review". *Ocean Engineering,* **213**, p. 107768.

[4] Today, O. E., 27 March, 2019. "eni's new wave power device to convert mature offshore platforms into renewable energy hubs,". Accessed: January 31, 2021.

[5] Oliveira-Pinto, S., Rosa-Santos, P., and Taveira-Pinto, F., 2019. "Electricity supply to offshore oil and gas platforms from renewable ocean wave energy: Overview and case study analysis". *Energy Conversion and Management,* **186**, pp. 556–569.

[6] Bull, A. S., and Love, M. S., 2019. "Worldwide oil and gas platform decommissioning: a review of practices and reefing options". *Ocean & coastal management,* **168**, pp. 274–306.

[7] Jonkman, J., Butterfield, S., Musial, W., and Scott, G., 2009. Definition of a 5-mw reference wind turbine for offshore system development. Tech. rep., National Renewable Energy Lab.(NREL), Golden, CO (United States).

[8] Bureau of Safety and Environmental Enforcement, FEB, 2021. "platform structures online query,". Accessed: February 1, 2021.

[9] Babarit, A., Hals, J., Muliawan, M. J., Kurniawan, A., Moan, T., and Krokstad, J., 2012. "Numerical benchmarking study of a selection of wave energy converters". *Renewable energy,* **41**, pp. 44–63.

[10] Muliawan, M. J., Karimirad, M., and Moan, T., 2013. "Dynamic response and power performance of a combined spar-type floating wind turbine and coaxial floating wave energy converter". *Renewable Energy,* **50**, pp. 47–57.

[11] Karimirad, M., and Koushan, K., 2016. "Windwec: Combining wind and wave energy inspired by hywind and wavestar". In 2016 IEEE International Conference on Renewable Energy Research and Applications (ICRERA), IEEE, pp. 96–101.

[12] Cheng, Z., Wen, T. R., Ong, M. C., and Wang, K., 2019. "Power performance and dynamic responses of a combined floating vertical axis wind turbine and wave energy converter concept". *Energy,* **171**, pp. 190–204.

[13] Michailides, C., 2021. "Hydrodynamic response and produced power of a combined structure consisting of a spar and heaving type wave energy converters". *Energies,* **14**(1), p. 225.

[14] Babarit, A., 2015. "A database of capture width ratio of wave energy converters". *Renewable Energy,* **80**, pp. 610–628.

[15] Wan, L., Gao, Z., and Moan, T., 2015. "Experimental and numerical study of hydrodynamic responses of a combined wind and wave energy converter concept in survival modes". *Coastal Engineering,* **104**, pp. 151–169.

[16] Suzuki, H., and Sato, A., 2007. "Load on turbine blade in-

Downloaded from http://asmedigitalcollection.asme.org/IDETC-CIE/proceedings-pdf/IDETC-CIE2022/86311/V010T10A013/6944006/v010t10a013-detc2022-91322.pdf by Michigan State University, Wei Che Tai on 05 October 2023

Copyright © 2022 by ASME

duced by motion of floating platform and design requirement for the platform". In International Conference on Offshore Mechanics and Arctic Engineering, Vol. 42711, pp. 519–525.

[17] Yue, M., Liu, Q., Li, C., Ding, Q., Cheng, S., and Zhu, H., 2020. "Effects of heave plate on dynamic response of floating wind turbine spar platform under the coupling effect of wind and wave". *Ocean Engineering,* **201**, p. 107103.

[18] Koo, B., Kim, M., and Randall, R., 2004. "Mathieu instability of a spar platform with mooring and risers". *Ocean engineering,* **31**(17-18), pp. 2175–2208.

[19] Subbulakshmi, A., and Sundaravadivelu, R., 2016. "Heave damping of spar platform for offshore wind turbine with heave plate". *Ocean Engineering,* **121**, pp. 24–36.

[20] Liang, C., 2016. "On the dynamics and design of a wave energy converter with mechanical motion rectifier". PhD thesis, State University of New York at Stony Brook.

[21] Gupta, A., and Tai, W.-C., 2022. "The response of an inerter-based dynamic vibration absorber with a parametrically excited centrifugal pendulum". *Journal of Vibration and Acoustics*, pp. 1–39.

[22] Liang, C., Ai, J., and Zuo, L., 2017. "Design, fabrication, simulation and testing of an ocean wave energy converter with mechanical motion rectifier". *Ocean Engineering,* **136**, pp. 190–200.

[23] Seebai, T., and Sundaravadivelu, R., 2013. "Response analysis of spar platform with wind turbine". *Ships and Offshore Structures,* **8**(1), pp. 94–101.

[24] Mérigaud, A., 2018. "A harmonic balance framework for the numerical simulation of non-linear wave energy converter models in random seas". PhD thesis, National University of Ireland, Maynooth (Ireland).

[25] Cummins, W., Iiuhl, W., and Uinm, A., 1962. "The impulse response function and ship motions".

[26] Ogilvie, T. F., 1964. "Recent progress toward the understanding and prediction of ship motions". In 5th ONR Symp. on Naval Hydrodynamics.

[27] Yeung, R. W., 1981. "Added mass and damping of a vertical cylinder in finite-depth waters". *Applied Ocean Research,* **3**(3), pp. 119–133.

[28] Hatwal, H., Mallik, A., and Ghosh, A., 1983. "Forced nonlinear oscillations of an autoparametric system—part 1: periodic responses".

[29] Song, Y., Sato, H., Iwata, Y., and Komatsuzaki, T., 2003. "The response of a dynamic vibration absorber system with a parametrically excited pendulum". *Journal of Sound and Vibration,* **259**(4), pp. 747–759.

[30] Warminski, J., and Kecik, K., 2009. "Instabilities in the main parametric resonance area of a mechanical system with a pendulum". *Journal of Sound and Vibration,* **322**(3), pp. 612–628.

[31] Sharif-Bakhtiar, M., and Shaw, S., 1992. "Effects of nonlinearities and damping on the dynamic response of a centrifugal pendulum vibration absorber".

[32] Cameron, T., and Griffin, J. H., 1989. "An alternating frequency/time domain method for calculating the steady-state response of nonlinear dynamic systems".

[33] Detroux, T., Renson, L., Masset, L., and Kerschen, G., 2015. "The harmonic balance method for bifurcation analysis of large-scale nonlinear mechanical systems". *Computer Methods in Applied Mechanics and Engineering,* **296**, pp. 18–38.

[34] Xie, L., Baguet, S., Prabel, B., and Dufour, R., 2017. "Bifurcation tracking by harmonic balance method for performance tuning of nonlinear dynamical systems". *Mechanical Systems and Signal Processing,* **88**, pp. 445–461.

[35] Kristiansen, E., Hjulstad, Å., and Egeland, O., 2005. "State-space representation of radiation forces in time-domain vessel models". *Ocean Engineering,* **32**(17-18), pp. 2195–2216.

Downloaded from http://asmedigitalcollection.asme.org/IDETC-CIE/proceedings-pdf/IDETC-CIE2022/86311/V010T10A013/6944006/v010t10a013-detc2022-91322.pdf by Michigan State University, Wei Che Tai on 05 October 2023

Copyright © 2022 by ASME